

A Hybrid Class Underwater Vehicle: Bioinspired Propulsion, Embedded System, and Acoustic Communication and Localization System

AUTHORS

Michael Krieg

Peter Klein

Robert Hodgkinson

Department of Mechanical and Aerospace Engineering, University of Florida

Kamran Mohseni¹

Departments of Mechanical and Aerospace Engineering and Computer Engineering, Institute for Cyber Autonomous Systems, University of Florida

ABSTRACT

Inspired by the natural locomotion of jellyfish and squid, a series of compact thrusters series is developed for propulsion and maneuvering of underwater vehicles. These thrusters successively ingest and expel jets of water in a controlled manner at high frequencies to generate propulsive forces. The parameters controlling the performance of the thrusters are reviewed and investigated to achieve higher thrust levels. The thrusters are compact and can be placed completely inside a vehicle hull providing the desired maneuvering capability without sacrificing a sleek hydrodynamic shape for efficient cruising. The system design of a prototype hybrid vehicle, called CephaloBot, utilizing these thrusters, is also presented. A compact and custom-developed embedded system is also designed for the CephaloBot. Key features of the system include a base set of navigational sensors, an acoustic system for localization and underwater communication, Xbee RF transceiver for communication above water, and a LabVIEW programmed processing board.

Keywords: AUV, thruster, bioinspired, communication

Introduction

Traditionally unmanned underwater vehicles fall into one of two categories. One class of vehicles (torpedo like) are built to travel long distances with minimal energy and are usually characterized by a long slender body, a rear propeller for propulsion and a set of fins to provide maneuvering forces. This type of vehicle is poorly suited for missions requiring a high degree of positioning accuracy because the control surfaces provide little to no maneuvering force at low forward velocity. The other class of vehicle similar to remotely operated vehicles (ROVs) is designed to operate in these situations, which do require

high positioning accuracy, and incorporate several thrusters at various locations to provide maneuvering forces in all directions. However, this class of vehicle typically has a very high drag coefficient due to the abundance of external thrusters and cannot travel to remote locations without additional support.

The abundance of remote marine research sites requiring high positioning accuracy for inspection, as well as the desire to create fully autonomous vehicle sensor networks, has inspired significant research in a hybrid class of vehicles with the efficient cruising characteristics of the torpedo class and the maneuvering abilities of the ROV class. Some take a mechanical approach moving the maneuvering

propellers into tunnels which run through the hull of the vehicle (McLean, 1991; Torsiello, 1994) or into the fins themselves (Dunbabin et al., 2005). Others observe that nature's swimmers have a healthy balance of long-distance endurance and high-accuracy low-speed maneuvering. Vehicles have been designed to use fins for both high-speed maneuvering as well as mimic the low-speed flapping of turtles and marine mammals (Licht et al., 2004; Licht, 2008; Kato, 2011); and some use tail fins as a primary means of propulsion (Barrett et al., 1999). Our inspiration comes from the cyclical jet propulsion seen in jellyfish, scallops, octopus, squid and other cephalopod. Squid jet propulsion produces the fastest swimming

¹This work was started while the group was at the University of Colorado.

velocities seen in aquatic invertebrates (O’Dor & Webber, 1991; Anderson & Grosenbaugh, 2005).

Jetting locomotion begins when the squid inhales seawater through a pair of ostia behind the head, filling the mantle cavity (see Figure 1). The mantle then contracts forcing seawater out through the funnel that rolls into a high-momentum vortex ring and imparts the necessary propulsive force (Anderson & Grosenbaugh, 2005). The versatility of the system permits two distinct gaits, cruising and escape jetting (Bartol et al., 2008). During cruising, squid swim at nominal speed with a greater efficiency than escape jetting, which involves a hyper-inflation of the mantle followed by a fast powerful contraction to impart significant acceleration at the cost of both muscular and fluid dynamic losses. Bartol et al. (2009) report cruising mode efficiency at 69% ($\pm 14\%$) averaged over several species and swimming speeds and 59% ($\pm 14\%$) for escape jetting. Additionally, propulsive efficiency was seen to rise as high as 78% in adult *L. brevis* swimming at high velocities and averaged 87% ($\pm 6.5\%$) for paralarvae (Bartol et al., 2008), challenging the notion that a low-volume high-velocity jet inherently negates a high propulsive efficiency.

The locomotion of jellyfish tends to be very similar to that of squid with some key differences, primarily that the refilling phase of jellyfish

swimming uses the same bell opening as the jetting phase. Despite the fact that squid do not use the funnel during refilling, the inlet vents are still on the anterior side of the mantle cavity, meaning that locomotion for both organisms is quite different from traditional pumping mechanisms. Jellyfish use the cyclic jetting process for feeding as well as locomotion as is evidenced by Lagrangian coherent structures and particle tracer analysis (Lipinski & Mohseni, 2009; Wilson et al., 2009); in addition, both squid and jellyfish utilize jetting for respiration, taking advantage of the large fluid flow rates. Both of these factors can make it difficult to determine which swimming behaviors are optimized for propulsion versus secondary functions. Similar to the different gaits seen in squid locomotion, different species of jellyfish generally fall into two categories of swimmers based on the ‘quality’ of vortex ring they produce. Jellyfish like moon jellyfish have a very large bell opening, and the jetting motion is similar to a paddling type motion. Box jellyfish and other faster swimming jellyfish have smaller bell openings with nozzle-like flaps and have a much more distinct jet. Jellyfish morphology during swimming has been digitally captured from experiment, and the body motions were imported into numerical simulations to predict body forces on the swimming jellyfish, determining drastically different swimming efficiencies.

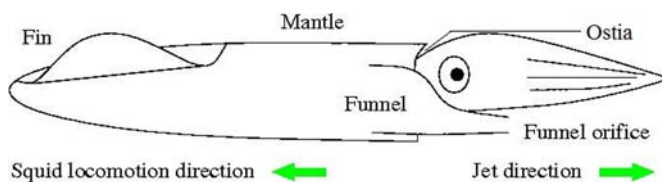
Froude propulsive efficiency of jellyfish was directly calculated by Sahin and Mohseni (2008, 2009; Sahin et al., 2009) to be 37% for *Aequorea victoria* and 17% for *Sarsia tubulosa*. It should be noted that both species of jellyfish most likely do not use vortex generation for the sole purpose of locomotion. *Aequorea victoria* uses vortex generation for feeding and *Sarsia tubulosa* as an escape mechanism. Empirical data gathered through digital particle image velocimetry (DPIV) measurements of several species shows similar efficiency characteristics for the different swimming patterns (Dabiri et al., 2010).

The general concept of propelling water craft by ejecting a high-velocity water jet is centuries old, was hypothesized by both Bernoulli and Benjamin Franklin, and was utilized in a rudimentary sense in one of the first steam boat designs by James Rumsey (Allen, 2010). Continuously pumped jets are used for propulsion in modern water craft-like jet skis and bow thrusters of motorboats; however, this type of jet propulsion is inherently different from the propulsion of squid and jellyfish, which create distinct vortex rings. The thrusters of this paper also produce finite jets, which form arrays of vortex rings, and should be considered fundamentally different than continuous jet thrusters.

This paper showcases a complete hybrid class vehicle that demonstrates added maneuvering capabilities utilizing a set of bio-inspired jet thrusters. The manuscript will focus on three primary systems of the vehicle: a bio-inspired thruster system and fundamentals of thruster mechanics, an acoustic system, which serves the dual purpose of communication and localization, and a compact embedded control system. The manuscript is

FIGURE 1

Diagram of squid layout and locomotion.



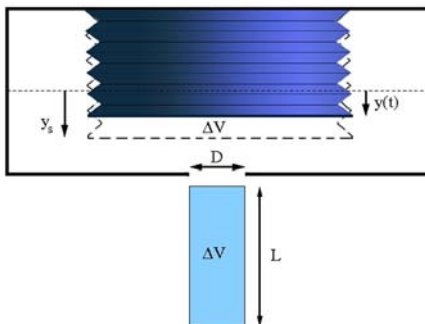
organized as follows. The mechanics of the thruster as well as the thrust dynamics are described in ‘Vortex Ring Thrusters’ section. A brief history of thruster and vehicle prototypes is given in ‘Thruster and CephaloBot Evolution’. The ‘Hybrid Vehicle Description’ section gives basic requirements for a hybrid class vehicle, and the subsystem components of CephaloBot are described in more details in ‘Communication Localization System’, ‘Embedded System’, and ‘Sensors’ sections.

Vortex Ring Thrusters

Our thruster inspired by jellyfish and squid propulsion consists of an internal fluid cavity, with a semi-flexible plunger used to drive fluid motion, and a small circular orifice exposed to the external fluid. See Figure 2 for a diagram of the thruster layout. The cavity of the thruster provides the same functionality as the squid mantle or the jellyfish bell, expanding and contracting to cycle water in and out of the circular orifice (functionally similar to the squid funnel/siphon). Since the thruster generates propulsion by creating energetic vortex rings, it

FIGURE 2

Conceptual diagram of the thruster key components. Jet shown as hypothetical slug of fluid.



is termed the ‘vortex ring thruster’ (VRT).

Since VRTs are contained internal to the vehicle (with only a small opening on the vehicle surface), they do not significantly affect the vehicle’s forward drag profile, which means that a vehicle equipped with a set of VRTs for low-speed maneuvering and a rear propeller for primary propulsion will have a sleek aerodynamic shape allowing fast efficient cruising to a site of interest but still maintain full maneuverability (even at zero forward speed) upon reaching that site of interest. See Krieg and Mohseni (2010) for ‘parallel parking’ capability of an earlier version of our vehicle. Additionally, since the VRT only needs a single opening (unlike tunnel thrusters or traditional pumps, which extend from one end of the hull to the other), it allows for a greater degree of freedom for internal system arrangement.

The impulse generated by this type of device can be modeled as if the jet acts like a solid slug of fluid with a uniform velocity across the nozzle opening (Mohseni, 2004, 2006; Krieg & Mohseni, 2008). Properties of fluid slug have been investigated by several groups (Glezer, 1988; Gharib et al., 1998; Shariff & Leonard, 1992; Mohseni & Gharib, 1998; Krieg & Mohseni, 2008). The total impulse generated for a single pulsation under slug assumptions is

$$I_{slug}(t) = \rho\pi/4 \int_0^t u^2(\tau) D^2 d\tau, \quad (1)$$

where u is the piston velocity (mass flux across thruster opening divided by nozzle area), D is the nozzle Diameter, ρ is the fluid density, t is the time at which the impulse is evaluated, and τ is a dummy variable for time initialized at the beginning of pulsation.

Krueger and Gharib (2003) showed that the impulse created by a cylinder piston type vortex generator was consistently higher than the impulse predicted by the slug model. This added impulse was attributed to a pressure gradient at the nozzle exit plane, referred to as ‘nozzle overpressure.’ Adding I_p (the impulse due to overpressure), we get an equation for the impulse, in terms of the nozzle pressure, p (which is a function of time and radial position), and the stagnation pressure, p_∞ .

$$I(t) = I_{slug}(t) + I_p(t)$$

$$I_p(t) = \int_0^t \int_A [p(r, \tau) - p_\infty] dAd\tau \quad (2)$$

We performed initial testing on a thruster which periodically ingested and expelled jets with a sinusoidal velocity program; which was chosen for simplicity of fabrication. Assuming that there is no net momentum transfer during the ingestion phase (fluid being taken into the cavity starts at rest outside of the thruster and ends at rest inside the cavity) and ignoring the pressure impulse (which will be accounted for with a coefficient term post analysis), then the average thrust produced over a full cycle can be calculated in terms of the thruster frequency to be (Krieg & Mohseni, 2008)

$$\bar{T} = \frac{\rho\pi^3}{16} D^4 \left(\frac{L}{D}\right)^2 f^2 \quad (3)$$

Here f is the frequency of actuation, and the term L/D is the jet stroke ratio. If the jet maintained its shape as a solid cylinder the stroke ratio would be the ratio of length to diameter of that cylinder (see Figure 2). The stroke ratio has also been called the formation

time since it is equivalent to the time since initiation of the jet flow scaled by jet velocity and nozzle diameter, $t^* = L/D = \int_0^t u(\tau) dt / D$. The formation time is closely related to the jet formation dynamics. When a jet is expelled into a stationary fluid, the viscous forces cause the initial portion of the jet to roll into a tightly wound vortex ring. As more fluid is expelled, it feeds the growing vortex ring until a critical saturation point is reached and the vortex ring can no longer support the added circulation. At this point, the vortex ring separates from the remaining shear flow. The formation time when the jet has achieved the same circulation as the final vortex ring is known as the formation number. Gharib et al. (1998) demonstrated that impulsively started vortex rings have a universal formation number ($\approx 3.6-4.2$) independent of jet velocity and diameter. However, numerical studies have shown the formation number to be drastically lower for jets created with a parabolic velocity profile (Rosenfeld et al., 1998) or a 2-D jet velocity like those produced in conical nozzles (Rosenfeld et al., 2009).

The slug model predicts that the average thrust is proportional to both the square of the actuation frequency and the square of the stroke ratio/formation time. To test this assertion, the thruster was placed in a static fluid reservoir and suspended from a load cell, and the thrust output was measured directly. This testing setup is shown in Figure 3 (Krieg & Mohseni, 2008). It should be noted that if the vehicle is moving during thruster pulsation there will inherently be a non-zero momentum transfer during ingestion; however, as was previously mentioned these thrusters are primarily intended for low-speed maneu-

FIGURE 3

Thruster static testing environment.

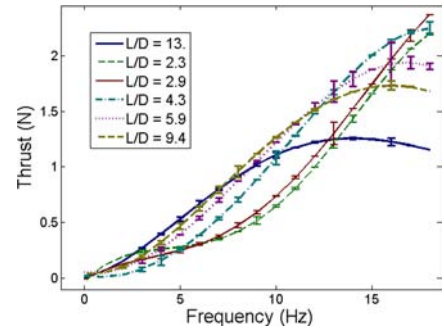


vering (vehicle velocities well below jetting velocities), so that the momentum transfer during ingestion will still be negligible compared to the momentum transfer of the jetting phase. In addition, the expelled jet rolls into an isolated vortex ring which inherently produces a large momentum transfer associated with the fluid impulse of the vortex ring itself. During ingestion, the small internal cavity severely limits vortex ring formation as well as momentum transfer associated with it.

The thruster was tested over a wide range of stroke ratios and actuation frequencies. As can be seen in Figure 4, the thrust shows a square proportionality to frequency, within a certain frequency range. When producing jets with low stroke ratio, this range is the entire sub-cavitation frequency range. However, when the jet stroke ratio goes above the formation number, the thruster exhibits a parabolic dependence on the actuation frequency after a short range of square dependence. To more clearly show this trend, we define a scale factor, which

FIGURE 4

Thrust versus frequency. Each set of markers shows thrust data for a different stroke ratio. The error bars plotted along with the thrust relationship represent a single standard deviation of the thrust data.

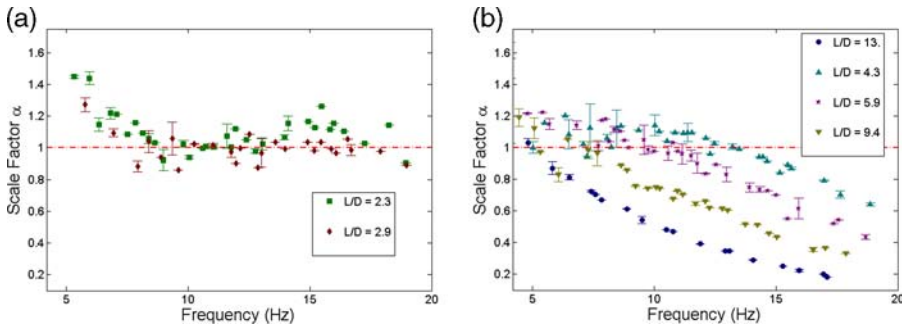


is a measure of the accuracy of the slug model for various operating conditions $\alpha = T_{Exp} / \bar{T}$ (Krieg & Mohseni, 2008) where \bar{T} is the slug model predicted average thrust from equation (3). This scale factor is plotted with respect to frequency for stroke ratios below the formation number in Figure 5a and for stroke ratios above the formation number in Figure 5b. Note that the thruster of this study has a nozzle which is essentially a flat plate with a circular orifice in the middle. This type of nozzle produces a 2-D jet flow similar to a conical nozzle, meaning that the jet formation number is closer to 3 (Rosenfeld et al., 2009). For a more in depth analysis of the shift in formation number due to the 2-D aspect of the jet, see Krieg and Mohseni (2011).

First, consider the thrust response of the actuator operating below the formation number (Figure 5a). In the low-frequency regime, the scale factor is higher than that predicted by the slug model due to the nozzle overpressure, reaching 1.4 times the predicted value. Krueger and Gharib (2003) showed that the pressure impulse can reach as much as 40% of the total

FIGURE 5

Scale factor (slug model accuracy) versus frequency for stroke ratios below (a) and above (b) the formation number. Error bars shown on data points indicate a standard deviation of measured values at that frequency (also taken in the scaled space).



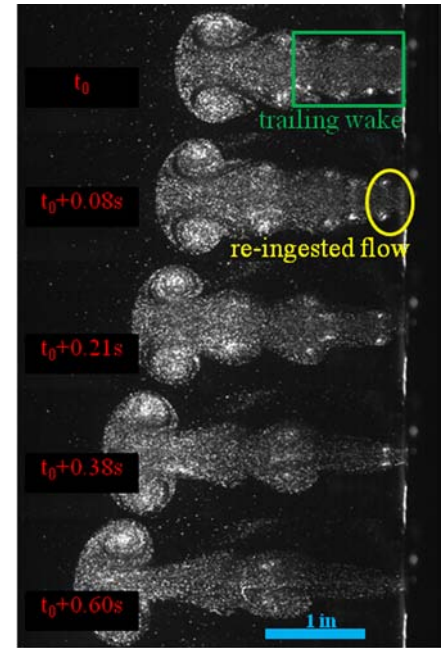
impulse for low stroke ratio jets corresponding to a total impulse 1.6 times the predicted slug model impulse. However, as the frequency increases, the total thrust settles on the value predicted by the slug model, meaning that in this frequency range the impulse due to overpressure during expulsion is equal to the impulse due to “underpressure” during refilling so that the net impulse transfer is that predicted by the slug model. Now consider the thruster response when operating above the formation number, shown in Figure 5b. Again the low-frequency ranges exhibit an added impulse due to the nozzle overpressure; albeit to a lower extent as observed by Krueger and Gharib (2003). But the high-frequency range exhibits an added loss in thrust with respect to the slug model prediction. This relative loss is seen to increase monotonically with both actuation frequency and stroke ratio. This suggests that another assumption made in the slug model is no longer valid when operating above the formation number. We assume that this loss in model accuracy is tied into the assumption made that all fluid being ingested between pulsations is at rest outside of the thruster. When a jet is ejected with a stroke ratio above the

formation number, some of the shear flow is left behind in the trailing wake of the leading vortex ring. The trailing wake has a lower momentum than the leading vortex ring and travels at a much lower induced velocity but still has a forward momentum substantially larger than the surrounding resting fluid. Therefore, the loss in slug model accuracy could be explained by the thruster ingesting some of the trailing wake during the refilling phase. Figure 6 shows successive frames from a video of the thruster’s forming jet (at a high stroke ratio) where some of the trailing wake is ingested back into the thruster.

It should also be noted that the scale factor results are only presented above an actuation frequency of 4 Hz, because the thruster was designed to operate cyclically rather than generate individual pulsations. The 2-D nature of the jet created by this type of thruster (orifice nozzle) has an added effect on the nozzle overpressure not seen in the frequency ranges presented. This effect is fully explained (along with a more in depth description of impulse generation) for a single pulsation with constant jet velocity in Krieg and Mohseni (2011). Despite the relative magnitude of the overpressure

FIGURE 6

Successive frames of jet flow showing the thruster re-ingesting wake flow.



impulse (with respect to the momentum impulse, I_{slug}), it is only observed in low actuation frequencies, which are coupled with low thrust output. Often vehicle mission scenarios will necessitate a large magnitude thrust output (higher actuation frequencies), where the overpressure is cancelled out, and the slug model provides an accurate thrust measurement.

The vortex ring formation phenomenon plays a key role in the jet locomotion process in squid as well. Bartol et al. (2009) observed that squid have two distinct swimming gaits. In the efficient cruising gait jets are expelled below the formation number, so that the majority of the jet rolls into the primary vortex ring. Alternatively, in threatening situations the squid employs a swimming technique referred to as escape jetting; which begins with the hyperinflation of the mantle followed by a fast contraction expelling a jet well above the formation number.

Presumably this behavior indicates that this type of jet propulsion is most efficient when expelling jets below the formation number and that jetting above the formation number can achieve higher thrust at the expense of fluid losses.

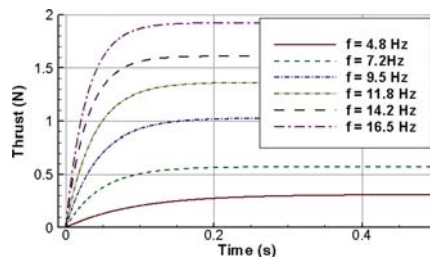
Therefore, all subsequent vehicle thrusters have been designed with a set diameter resulting in a stroke ratio near the formation number; to achieve a maximum level of thrust, while still being accurately described by the slug model. It should be noted that the formation number for a jet created on a moving vehicle will not be the same as the formation number of the jet in the static setup. Krueger et al. (2006) showed that vortex rings formed in the presence of a uniform background co-flow have a lower formation number than vortex rings formed in a resting fluid. Since a moving vehicle will inherently induce a co-flow with the jetting direction, this effect must be taken into consideration. However, the reduction in formation number is proportional to the ratio between co-flow velocity and jet velocity; therefore, the low-frequency (low jet velocity) pulsation will experience pinch off at an earlier formation time, but the lower-frequency pulsation is also less effected by the dynamics of cyclic vortex ring formation.

One advantage of the VRT is that it produces a desired level of thrust almost instantaneously (Krieg & Mohseni, 2010). Propeller style thrusters suffer from a rise time associated with reaching the static thrust level after initiating rotation. This rise time is inversely proportional to the desired level of thrust and can be on the order of several seconds for low thrust levels (Fossen, 1991; Yoerger et al., 1990). VRTs also have a rise time associated with reaching the desired level of thrust, which is inversely proportional to the

level of thrust. However, this rise time is an order of magnitude smaller for VRTs. The exact thrust program as a function of time is sinusoidal, due to the nature of the thruster; however, using several thrust data sets to average out the dynamic component and fitting the average thrust to a basic logarithmic curve the mean rise time can be observed. The fitted curves for several operational frequencies, and a stroke ratio of 4.3 is shown in Figure 7.

FIGURE 7

Mean thrust produced at various frequencies (static desired thrust level) versus time. Rise time inversely proportional to thrust level.



Along with a minimal rise time, the VRT is also immune to a thrust lag seen in tunnel thrusters (McLean, 1991), where thrust continues to be exerted on the vehicle after the thruster has been terminated.

Thruster and CephaloBot Evolution

The compact thrusters used in vehicle testbeds to provide validation of static testing have taken a wide variety of forms. The first generation utilized a solenoid driving mechanism and a flexing diaphragm to expel fluid (Figure 8a). The solenoid driving mechanism suffered from reduced stroke at higher actuation frequencies as the solenoid stroke was load dependent.

All of the subsequent iterations have used mechanical driving mechanisms for better flexibility in adjusting the operation conditions. Gen. 2 (Figure 8b) used a completely flexible cavity in a fitted mold, whereas Gen. 3 and 4 switched to a semi-flexible cavity which was reinforced to ensure constant diameter but allow compression in height. Gen. 3 (Figure 8c) used a complicated encompassing cylindrical tube cam to drive cavity compression, but mechanical complexities and reliability issues caused us to simplify to a basic crank shaft design for Gen. 4 (Figure 8d). In the figure, this thruster is shown with an acrylic casing to allow the components to be seen. The vehicle ready thruster uses an aluminum casing (Clark et al., 2009).

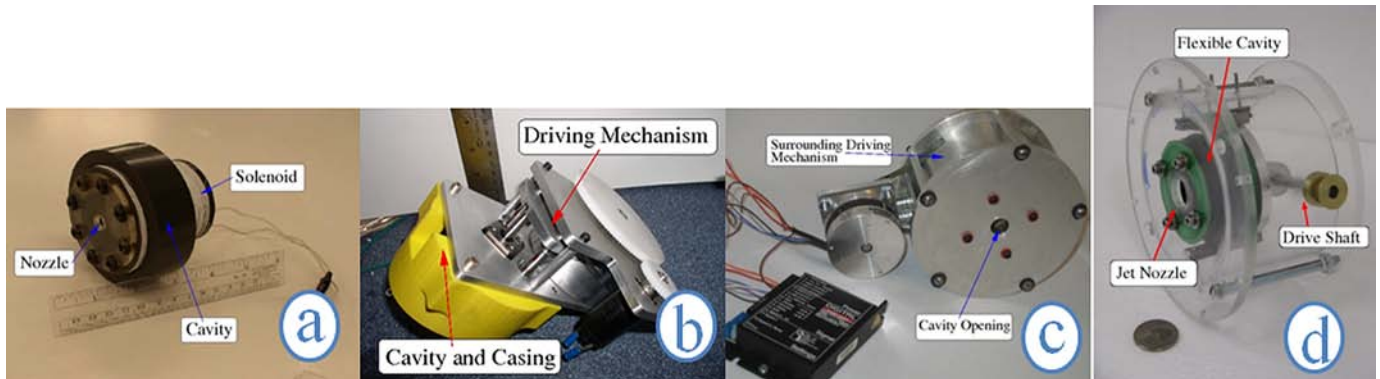
Along with the thrusters themselves the vehicle testbeds housing the thrusters have evolved rapidly. Figure 9 shows the evolution of vehicle testbeds used to demonstrate the feasibility of maneuvering using VRTs. Starting with the oldest vehicle at the bottom and successive generations upwards, the first vehicle only had fins to provide a standard for maneuvering capabilities, 2nd, 3rd and 4th generation vehicles contain 1st, 2nd and 3rd generation thrusters, respectively, and increasing levels of autonomy. The lessons learned from these vehicles directly lead to the development of the most recent hybrid class vehicle described in the following section.

Hybrid Vehicle Description

The newest generation of vehicle is intended to be used in autonomous sensor network applications. Therefore, the vehicle must be able to travel on long range missions collecting data

FIGURE 8

Successive generations of thrusters (a) utilize solenoid driver (7.5 cm/3-inch diameter), (b) utilize cavity and mold (10 cm/4-inch casing diameter), (c) have encompassing driving mechanism (12.5 cm/5-inch plate diameter) and (d) utilize simple crank shaft and semi-flexible ducting (10 cm/4-inch plate diameter).



but must also be capable of autonomously docking with permanent support structures. These structures will be responsible for downloading the vehicle's mission data, changing mission objectives and recharging vehicle batteries.

Autonomous docking with such a structure is a complicated problem, requiring not only high-accuracy maneuvering, but equally high-accuracy localization and attitude determination. In addition vehicles in this type of environment need to be capable of communicating with each other at short

distances for coordinated missions. In general reduction in cost and internal structure are also desirable to allow for more vehicles in the network with a wider range of payload options.

The base vehicle (Figure 10) is separated into three hull sections. The front and back sections house all of the actuators. Each section has two VRTs and an active buoyancy control device (BCD). Each thruster has an overall diameter of 7.6 cm (3 inches), a nozzle diameter of 1.8 cm (0.6 inch), has a stroke ratio of 4.5, and produces close to 2N of thrust at 30 Hz before cavitation starts to occur in the cavity. The back section also has the rear propeller motor. The primary batteries and all the electronics except motor control are housed in the center sec-

tion. An additional payload section may be added between front and center to include additional sensors, devices, and/or batteries. Regulated power and digital communication lines interface the payload to the center section. When put together, the 0.15 m (6 inches) diameter, 0.92 m (36 inches) long vehicle weighs a neutrally buoyant 16 kg (36 lb). The BCDs can change the buoyancy by $\pm 1\%$ to dive or surface, and 2 kg of internal ballast are adjustable to balance the pitch of the vehicle.

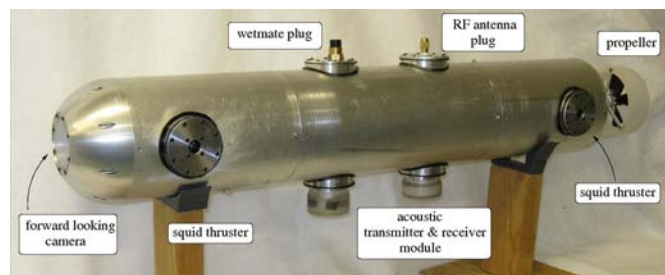
FIGURE 9

The first four generations of our vehicle test beds. Oldest vehicle at bottom, and successive vehicles placed in ascending order.



FIGURE 10

Fifth generation hybrid vehicle CephaloBot.



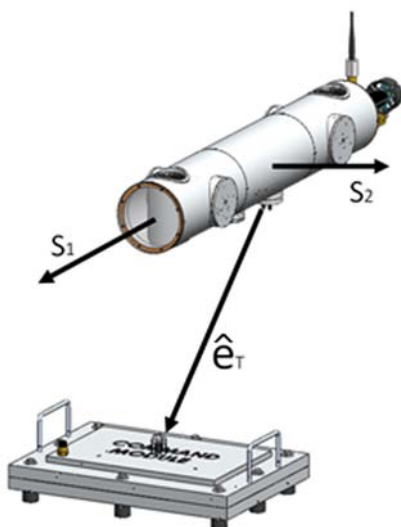
Communication/ Localization System

Due to the physical properties of water, RF communication methods

are not practical for small unmanned underwater vehicles. CephaloBot has a joint acoustic communication and localization system which is ideally suited for underwater sensor network applications. The communication technique is based on binary frequency modulation whereas the localization methodology is based on a time delay of arrival technique. The system consists of a specialized hydrophone array (fabricated in house as described later in this section), which interpret acoustic signals for both information and directional content. The receiving hydrophone array consists of three piezo electric ceramics spaced in a triangular arrangement parallel to the vehicle principle axis plane (Figure 11). Two piezo electric ceramics are placed on a line parallel to the pitching axis, and the 3rd is extended along the roll axis from the midpoint of the other two. The entire array is encased in urethane rubber with an acoustic impedance similar to water. The transmitting node consists of a single high-power piezo electric ceramic encased in the same type of urethane rubber as the

FIGURE 11

Definition of principle submarine axes.



hydrophone array. Each vehicle is equipped with both a receiving and transmitting node on the underside of the vehicle (see Figure 12).

FIGURE 12

Transducer nodes on the vehicle. Receiving node on the right and transmitting node on the left.



All three hydrophones in the receiving node receive a signal from a transmitting node (either on another vehicle or a docking station). The phase lag (ϕ) between the signal coming from the hydrophone on the roll axis and the signals coming from the two hydrophones on the pitching axis is measured and correlated with the signal frequency (f) to determine the time between when the hydrophones received the source signal $\Delta t_i = \phi_i/f$. The time lag is then multiplied by the speed of sound in water to get relative source distances in the vehicle frame and transformed into the inertial frame to get the azimuth and elevation of the receiving node with respect to the source node.

The hybrid localization/communication system is comprised of three main phases: data sending, data receiving and localization. Data receiving and localization both use the same incoming acoustic wave, the first 1000 cycles are dedicated to localization and the remaining cycles are frequency modulated. The acoustic wave propagates from a sending transducer located at some other node and

propagates towards the vehicle. Once this wave is received by the hydrophone array, it is conditioned by filtering and amplification circuitry. The conditioning circuitry contains a 17-dB gain pre-amplifier followed by two stages of filtering and two stages of amplification to bring the signal voltage to 5 V. The electrical voltage is then passed through exclusive or gates with one of the other signals (in the case of hydrophone 0, the signal is also passed to demodulation circuitry). During the localization portion of receiving an onboard microcontroller reads and stores the output of each of the three exclusive-or gates and also determines which of the three signals arrives first. The duty cycle of the exclusive-or gates directly relates to the phase difference of the signals. The localization hardware calculates and passes the azimuth and elevation angles (which define a cone of possible vehicle locations with the source node at the vertex) to the main navigation processor which uses secondary positioning sensors (depth sensor and electronic compass) to determine a unique solution to the position of the receiving node with respect to the transmitting node.

After the localization portion of receiving is complete the output of the exclusive-or gates are ignored and the microcontroller reads and stores the DC voltage level from a frequency to voltage converter which directly represents the frequency of the incoming frequency modulated signal.

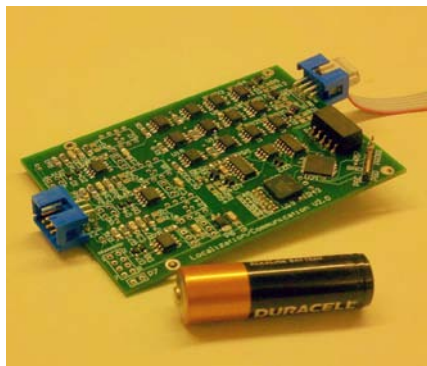
In order for the localization methodology to function properly the hydrophones must be placed no more than $\lambda/2$ apart where the wavelength λ is equal to the speed of propagation divided by the frequency ($\lambda = c/f$). This leads to a maximum spacing of 3 cm for a frequency of 25 kHz and 1.875 cm for a frequency of 40 kHz.

Miniature hydrophones which are approximately 1 cm in diameter are commercially available from Reson but are on the order of \$1000 per unit. Half-inch diameter cylindrical piezo electric ceramics (SMC14H12111) are available from Steminc for less than \$10/each. Placement of the three half-inch diameter piezo electric ceramics in a triangle pattern yields a maximum navigational frequency of 25 kHz. The sending and receiving transducers were made in house using a method similar to that in Li et al. (2010). The sending piezoceramic was chosen primarily based on its resonant frequency of 22 kHz and cylindrical shape to provide an omni-directional signal. The receiving hydrophone array and transmitter are shown placed on the belly of the CephaloBot in Figure 12.

Overall this customized communication localization system places a minimal load on the vehicle. The circuitry has a very small footprint (Figure 13) compared to typical commercial acoustic modems. In a two-way communication mode, the power draw is less than 1 W, and in simple listening mode, the power draw is less than 0.25 W. The transducers are fabricated in house so they can be customized to

FIGURE 13

Communication and localization hardware.



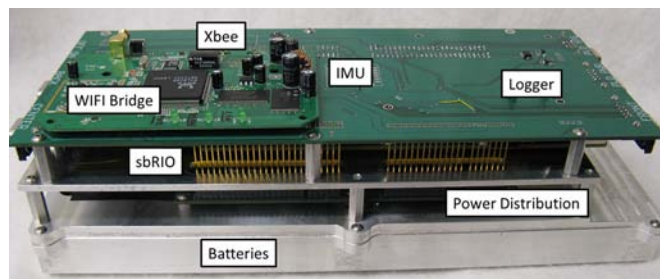
any shape and placed at any location on the vehicle to improve vehicle drag characteristics. The entire system is fabricated for under \$300 in materials, making it a suitable option for sensor networks requiring several low cost vehicles.

Embedded System

The embedded system was custom designed for the CephaloBot. The vehicle will be used by researchers for various underwater sensor networking applications and multi-vehicle coordination. In order to enable this underwater network to interact with a potential aerial sensor network, CephaloBot is also equipped with RF communication capabilities, spare computation power, and the ability to quickly add new sensors. Each vehicle must be robust and easy to handle and operate. The embedded system is separated into multiple printed circuit boards (PCB). A power distribution board handles voltage regulation and battery charging. An interface board connects the onboard devices and sensors with the power board and processing device. Smaller PCBs are located throughout the vehicle to provide specific functionality such as motor control, user interface, or simply wire routing. Figure 14 shows the electron-

FIGURE 14

Hybrid vehicle embedded system mounted on battery pack.



ics located in the center section, where everything except the motor controllers and user interface is located.

Processing

The primary processing device on the vehicle is a National Instruments Single-board RIO (sbRIO). It has an on-board 400 MHz processor running real-time LabVIEW software, 128 MB of RAM, 256 MB of flash, and a 40-MHz 2 M gate FPGA (field programmable gate array), also programmed in LabVIEW, providing 110 digital I/O pins. The combination of microprocessor and FPGA was proven effective in the 4th generation vehicle where a Compact RIO was used. All of the low-level communication, interface, and control tasks are handled on the FPGA, leaving the microprocessor open to perform high level mission control. The core vehicle software is located on the FPGA. The primary benefit is that the mission critical software will always run at full speed and safety checks will be implemented that a vehicle user cannot easily override. In this way, even if the algorithms being tested fail, the vehicle will remain safe to itself and surroundings. The 400-MHz real-time processor is little used by the core system and therefore provides significant computational power to the researcher. An

additional 2 GB of flash storage is added with a serial data logger and can be used for mission review.

Batteries

The power source is a four-cell lithium polymer pack. The nominal voltage of 14.8 V ranges from 10 to 16.8 V, depending on charge level. The lithium polymer chemistry was selected because of its high-power density and excellent discharge characteristics. A single four-cell battery pack was chosen because, during most of its discharge cycle, it will have a voltage between 14 and 16 V, which minimizes the voltage change of the high-current devices. The availability of integrated circuits and components for four-cell batteries was found to be better than an eight-cell approach, which would have a maximum voltage of 33.6 V and require larger 35 V tolerant components. Overall current required dictates some trace thicknesses of approximately 8 mm. The capacity of each cell is 21 Ah, which provides a total of 310 Wh for the pack. A commercial frontend battery circuit board protects the batteries from overcharging, over discharge, and short circuit. It also balances the cells to increase overall service life. The circuit has a very low resistance to have minimal impact on the efficiency. The charger built into the power distribution can charge the batteries in approximately 12 h. The high capacity of the batteries allows them to be discharged at a rate lower than 0.5 C, which increases battery runtime and overall lifetime (Murphy et al., 1990).

Power Distribution

The power distribution is the most complex custom-designed circuit board in the vehicle made into a four-layer

10 × 17 cm PCB. It regulates and monitors the voltages to power the rest of the electronics on the submarine.

The power distribution module uses a Microchip PIC18F45K22 as a microcontroller supervisor. This microcontroller monitors and controls voltages and current draws and parts or the whole system can be shut off if excessive current is drawn or voltages are not in an acceptable range. The presence of power sources is also monitored, and the microcontroller correctly decides which one to use and whether a battery requires charging. The sbRIO can signal the supervisor to enable or disable certain regulators on the vehicle to save power (i.e., wireless bridge is off when submerged). A function of the microcontroller also allows the vehicle to enter a “sleep” mode where everything except the supervisor microcontroller is turned off for a pre-determined period of time which reduces the total power usage to about 1 W. The microcontroller has an onboard analog-to-digital converter and a 16-channel multiplexer is used to read all of the required voltages and currents. Voltages are measured using a resistor-divider network to reduce the voltage into the multiplexer, and therefore the microcontroller to between 0 and 5 V with some error margin in case the voltage rises to more than intended. Allegro ACS714 Hall effect current sensors are used to provide very low loss method current measurements (0.06 W at 5 A).

Sensors

CephaloBot incorporates a minimum set of sensors needed to maintain a heading and depth underwater. Acoustics provide the vehicle with a relative position to a static pinger.

Intervehicle communication prevents collisions between vehicles and the walls of the pool. The vehicle is robust enough to withstand a collision if it does occur. When the vehicles are deployed to an ocean environment, payload sensors may be added heterogeneously to the vehicles and shared so that each submarine has all required data to successfully navigate its environment. To simplify the design, CephaloBot uses an all-in-one IMU solution from VectorNav. The device has an onboard three-axis accelerometer, gyroscope, and magnetometer. It performs Kalman filtering and outputs quaternions, Euler angles, and the raw sensor data to the sbRIO FPGA. The onboard filtering eliminates the need to develop or perform the computations on the sbRIO. Stated accuracies are less than 2°, and because a magnetometer provides an absolute reference, this accuracy will not degrade with time. A Honeywell pressure sensor provides fine resolution (0.01 m) measurements to 10-m depths. The device outputs an analog voltage. The test pool for the vehicle is 5-m deep, and so a higher resolution device as chosen over one that may be used to a deeper depth.

Conclusion

The CephaloBot provides an ideal low cost option for underwater sensor networking and hybrid vehicle applications. The vehicle has maneuvering capabilities at zero forward velocity necessary for docking and high-resolution sensing. This capability is provided by an array of novel squid and jellyfish inspired thrusters. The thrusters are located internal to the hull with only a small orifice exposed to the outer flow minimizing the effect on forward drag and allowing for efficient

high-speed transit. Additionally these thrusters only require the single opening, allowing for greater system freedom internal to the vehicle in-between thrusters.

The embedded controller system designed for the vehicle has a compact modular design allowing for a wide variety of possible mission objectives. The microcontroller, which is operated on an easily adaptable LabVIEW platform, includes several open connections for future mission operations, on top of the base level vehicle operation input/outputs. The vehicle also has a wide variety of communication options including a low cost and in house developed acoustic communication/localization system for communication between underwater vehicles and support structures. The vehicle has an RF system for communication with aerial vehicles while on the surface, and a WIFI bridge for communication with testers and data loggers while in controlled laboratory environments.

Acknowledgments

The authors would like to thank S. Lawrence-Simon, Tyler Thomas, Ryan Delgizzi, Dan Ambrosio, Colin Miller, Mikhail Kosna, and Matt Rhode for their hours of working on design and fabrication of the vehicle. We would also like to thank the Office of Naval Research (code 34) for funding this research project.

Corresponding Author:

Kamran Mohseni
231 MAE-A, Department of
Mechanical and Aerospace
Engineering
University of Florida, Gainesville, FL
Email: mohseni@ufl.edu

References

- Allen**, D.G. 2010. James Rumsey: Steamboat inventor or pioneer in steam navigation. Magazine of the Jefferson County Historical Society. 96:48-54.
- Anderson**, E., & Grosenbaugh, M. 2005. Jet flow in steadily swimming adult squid. J Exp Biol. 208:1125-46. doi: 10.1242/jeb.01507.
- Barrett**, D., Triantafyllou, M.S., Yue, D.K.P., Grosenbaugh, M.A., & Wolfgang, M.J. 1999. Drag reduction in fish-like locomotion. J Fluid Mech. 392:183-212. doi: 10.1017/S0022112099005455.
- Bartol**, I.K., Krueger, P.S., Stewart, W.J., & Thompson, J.T. 2009. Hydrodynamics of pulsed jetting in juvenile and adult brief squid *Lolliguncula brevis*: Evidence of multiple jet 'modes' and their implications for propulsive efficiency. J Exp Biol. 212:1889-903. doi: 10.1242/jeb.027771.
- Bartol**, I.K., Krueger, P.S., Thompson, J.T., & Stewart, W.J. 2008. Swimming dynamics and propulsive efficiency of squids throughout ontogeny. Integr Comp Biol. 48(6):720-33.
- Clark**, T., Klein, P., Lake, G., Lawrence-Simon, S., Moore, J., Rhea-Carver, B., ... Wu, A. 2009. Kraken: Kinematically roving autonomously controlled electro-nautic. In: Aerospace Sciences Meeting. Orlando, FL: AIAA.
- Dabiri**, J.O., Colin, S.P., Katija, K., & Costello, J.H. 2010. A wake based correlate of swimming performance and foraging behavior in seven co-occurring jellyfish species. J Exp Biol. 213:1217-75. doi: 10.1242/jeb.034660.
- Dunbabin**, M., Roberts, J., Usher, K., Winstanley, G., & Corke, P. 2005. A hybrid auv design for shallow water reef navigation. In: Proceedings of the International Conference on Robotics and Automation. pp. 2105-10. Barcelona, Spain: IEEE. doi: 10.1109/ROBOT.2005.1570424.
- Fossen**, T.I. 1991. Nonlinear modeling and control of underwater vehicles. Ph.D. thesis, Norwegian Inst. Technol., Trondheim, Norway.
- Gharib**, M., Rambod, E., & Shariff, K. 1998. A universal time scale for vortex ring formation. J Fluid Mech. 360:121-40. doi: 10.1017/S0022112097008410.
- Glezer**, A. 1988. The formation of vortex rings. Phys Fluids. 31(12):3532-42. doi: 10.1063/1.866920.
- Kato**, N. 2011. Swimming and walking of an amphibious robot with fin actuators. Mar Technol Soc J. 45(4):181-97.
- Krieg**, M., & Mohseni, K. 2008. Thrust characterization of pulsatile vortex ring generators for locomotion of underwater robots. IEEE J Oceanic Eng. 33(2):123-32. doi: 10.1109/JOE.2008.920171.
- Krieg**, M., & Mohseni, K. 2010. Dynamic modeling and control of biologically inspired vortex ring thrusters for underwater robot locomotion. IEEE T Robot. 26(3):542-54. doi: 10.1109/TRO.2010.2046069.
- Krieg**, M., & Mohseni, K. 2011. Thrust enhancement from radial velocity in squid inspired thrusters. OCEANS 2011, in press. Kona, HI: MTS/IEEE.
- Krueger**, P.S., Dabiri, J., & Gharib, M. 2006. The formation number of vortex rings formed in a uniform background co-flow. J Fluid Mech. 556(1):147-66. doi: 10.1017/S0022112006009347.
- Krueger**, P.S., & Gharib, M. 2003. The significance of vortex ring formation to the impulse and thrust of a starting jet. Phys Fluids. 15(5):1271-81. doi: 10.1063/1.1564600.
- Li**, Y., Kastner, R., Faunce, B., Domond, K., Kimball, D., Schurgers, C., & Benson, B. 2010. Design of a low-cost underwater acoustic modem. IEEE ESL. 2:58-61. doi: 10.1109/LES.2010.2050191.
- Licht**, S. 2008. Biomimetic oscillating foil propulsion to enhance underwater vehicle agility and maneuverability. Ph.D. thesis, Massachusetts Institute of Technology, Cambridge, Massachusetts.
- Licht**, S., Polidoro, V., Flores, M., Hover, F., & Triantafyllou, M. 2004. Design and projected performance of a flapping foil

- aav. IEEE J Oceanic Eng. 29(3):786-68. doi: 10.1109/JOE.2004.833126.
- Lipinski, D., & Mohseni, K.** 2009. A numerical investigation of flow structures and fluid transport with applications to feeding for the hydromedusae *Aequorea victoria* and *Sarsiatubulosa*. J Exp Biol. 212:2436-47. doi: 10.1242/jeb.026740.
- Mclean, M.** 1991. Dynamic performance of small diameter tunnel thrusters. Ph.D. thesis, Naval Postgraduate School, Monterey, California.
- Murphy, T., Cason-Smith, D., James, S., & Smith, P.** 1990. Characterization of aa size lithium rechargeable cells. In: Power Sources Symposium, Proceedings of the 34th International. pp. 176-80. Cherry Hill, NJ: IEEE.
- Mohseni, K.** 2004. Zero-mass pulsatile jets for unmanned underwater vehicle maneuvering. In: 3rd "Unmanned Unlimited" Technical Conference, Workshop and Exhibit. pp. 2004-3686. Chicago, IL: AIAA.
- Mohseni, K.** 2006. Pulsatile vortex generators for low-speed maneuvering of small underwater vehicles. Ocean Eng. 33(16):2209-23.
- Mohseni, K., & Gharib, M.** 1998. A model for universal time scale of vortex ring formation. Phys Fluids. 10:2436-8. doi: 10.1063/1.869785.
- O'Dor, R.K., & Webber, D.** 1991. Invertebrate athletes: Trade-offs between transport efficiency and power density in cephalopod evolution. J Exp Biol. 160:93-112.
- Rosenfeld, M., Katija, K., & Dabiri, J.O.** 2009. Circulation generation and vortex ring formation by conical nozzles. J Fluids Eng. 131, 091204:1-8.
- Rosenfeld, M., Rambod, E., & Gharib, M.** 1998. Circulation and formation number of laminar vortex rings. J Fluid Mech. 376:297-318.
- Sahin, M., & Mohseni, K.** 2008. The numerical simulation of flow patterns generated by the hydromedusa *Aequorea victoria* using an arbitrary Lagrangian- Eulerian formulation. In: 38th Fluid Dynamics Conference and Exhibit. pp. 2008-3715. Seattle: AIAA.
- Sahin, M., & Mohseni, K.** 2009. An arbitrary Lagrangian-Eulerian formulation for the numerical simulation of flow patterns generated by the hydromedusa *Aequorea Victoria*. J Comp Physiol. 228:4588-605. doi: 10.1016/j.jcp.2009.03.027.
- Sahin, M., Mohseni, K., & Colins, S.** 2009. The numerical comparison of flow patterns and propulsive performances for the hydromedusae *Sarsia tubulosa* and *Aequorea Victoria*. J Exp Biol. 212:2656-67. doi: 10.1242/jeb.025536.
- Shariff, K., & Leonard, A.** 1992. Vortex rings. Annu Rev Fluid Mech. 34:235-79. doi: 10.1146/annurev.fl.24.010192.001315.
- Torsiello, K.** 1994. Acoustic positioning of the NPS autonomous underwater vehicle (AUV II) during hover conditions. Master's thesis, Naval Postgraduate School, Monterey, California.
- Wilson, M.M., Peng, J., Dabiri, J.O., & Eldridge, J.D.** 2009. Lagrangian coherent structures in low Reynolds number swimming. J Phys-Condens Mat. 21. Art. 204105. doi: 10.1088/0953-8984/21/20/204105.
- Yoerger, D., Cooke, J., & Slotine, J.J.** 1990. The influence of thruster dynamics on underwater vehicle behavior and their incorporation into control system design. IEEE J Oceanic Eng. 15(3):167-78. doi: 10.1109/48.107145.